Hyperspectral Face Recognition Under Variable Outdoor Illumination

Zhihong Pan, Glenn Healey, Manish Prasad, Bruce Tromberg[a]

Department of Electrical Engineering and Computer Science
[a]Beckman Laser Institute
University of California, Irvine, CA

ABSTRACT

We examine the performance of illumination-invariant face recognition in outdoor hyperspectral images using a database of 200 subjects. The hyperspectral camera acquires 31 bands over the 700-1000nm spectral range. Faces are represented by local spectral information for several tissue types. Illumination variation is modeled by low-dimensional spectral radiance subspaces. Invariant subspace projection over multiple tissue types is used for recognition. The experiments consider various face orientations and expressions. The analysis includes experiments for images synthesized using face reflectance images of 200 subjects and a database of over 7,000 outdoor illumination spectra. We also consider experiments that use a set of face images that were acquired under outdoor illumination conditions.

1. INTRODUCTION

Ideally, a face recognition system should identify human subjects under unconstrained conditions including variable illumination conditions and arbitrary face orientation and occlusion. Currently most face recognition systems discriminate human faces by analyzing geometric facial features.[1–5] Several of these systems have been successful on large databases acquired in controlled indoor environments.[6,7] The performance of these approaches, however, can be compromised when the face orientation changes or the subjects are imaged at different times.[6] Illumination variation can also cause performance degradation.[8] Detailed illumination models including illumination cone models[9] and geodesic illumination models[10] have been proposed for face recognition that is less sensitive to illumination variation. Thermal infrared imagery can also be used for illumination-invariant face recognition since thermal measurements have little dependence on the ambient illumination.[11] Geometric feature based algorithms have performed surprisingly well for face recognition under different indoor illumination conditions.[7] Under unknown outdoor illumination, however, the verification rate of the best systems can degrade by as much as 40%.[7] There is further performance degradation if pose variation and different illumination conditions are combined.[12]

Several sources of variability including face orientation and outdoor illumination can be addressed using methods that are based on spectral features. Hyperspectral imaging has been used in remote sensing applications[13] and the food industry[14] for several years. As hyperspectral cameras have become economically accessible, computational methods have been studied for face recognition. Previous work has shown that near-infrared (NIR) spectral properties of human tissue are different from person to person while remaining reasonably constant for different face orientations and over time.[15] This has allowed hyperspectral discriminants to perform well for recognition over a large database of faces acquired indoors under fixed illumination.[15]

In this paper, we present results on recognizing 200 human subjects under unknown outdoor illumination conditions in near infrared hyperspectral face images. A set of spectral reflectance images of the 200 subjects was used in the experiments. 7258 outdoor illumination spectra were used in conjunction with the spectral reflectance images to synthesize simulated outdoor hyperspectral images of the 200 subjects. A low-dimensional linear model for each tissue type for each subject was used to model the illumination variation in the reflected

Further author information: (Send correspondence to G. Healey)
G. Healey: E-mail: healey@ece.uci.edu; Z. Pan: E-mail: zpan@ece.uci.edu; M. Prasad: E-mail: mprasad@ece.uci.edu; B. Tromberg: E-mail: tromberg@bli.uci.edu

Algorithms and Technologies for Multispectral, Hyperspectral, and Ultraspectral Imagery X, edited by Sylvia S. Shen, Paul E. Lewis, Proceedings of SPIE Vol. 5425 (SPIE, Bellingham, WA, 2004) · 0277-786X/04/$15 · doi: 10.1117/12.543102

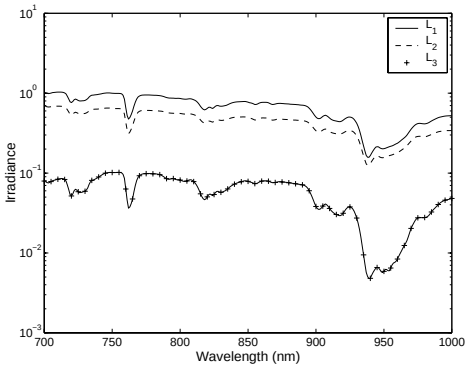

Figure 1. Global irradiance spectra $L(\lambda)$ measured at different times

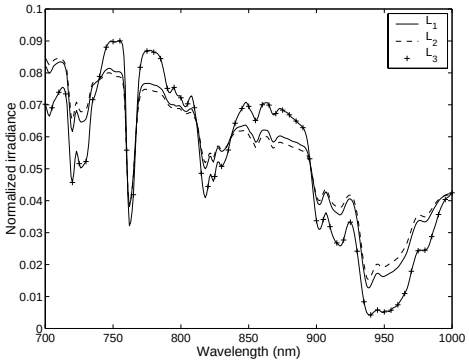

Figure 2. Normalized global irradiance spectra $L(\lambda)$ measured at different times

radiance spectra. Among the 200 subjects, ten subjects were imaged outdoors under unknown illumination conditions. For each subject, several near-infrared hyperspectral images with different facial expressions and face orientations were acquired on different days under various natural illumination conditions. Recognition under unknown illumination is achieved by projection from the measured hyperspectral image spectra onto the linear subspace models for the 200 subjects. We present a large set of results in recognizing the subjects under simulated outdoor illumination conditions using the synthesized images. We also present a set of results in recognizing the ten subjects against the database of 200 in images acquired under real outdoor illumination conditions.

2. REPRESENTING ILLUMINATION VARIABILITY

The near infrared illumination incident on a surface in an outdoor scene is described by the global spectral irradiance

$$L(\lambda) = T_d(\theta_o, \phi_o, \lambda) E_o(\lambda) cos(\theta_o) + \int \int E_s(\theta, \phi, \lambda) cos(\theta) sin(\theta) d\theta d\phi \quad (1)$$

where the coordinate system is defined by the azimuth angle ϕ in the tangent plane to the surface and the polar angle θ measured from the surface normal. $T_d(\theta_o, \phi_o, \lambda)$ is the atmospheric transmittance along the path from the sun to the surface, $E_o(\lambda)$ is the exoatmospheric solar radiance, (θ_o, ϕ_o) is the solar direction, $E_s(\theta, \phi, \lambda)$ is the scattered sky radiance from (θ, ϕ) and λ is wavelength. The integration in (1) is performed over the region of the hemisphere that is visible from the surface.

Among the terms in (1), T_d and E_s depend heavily on the atmospheric conditions and the time of day. Over the 0.7μm-1.0μm spectral range the atmospheric gases H_2O and O_2 produce significant absorption bands. Thus, T_d and E_s will vary according to the concentration of these gases which varies from place to place and over time. There is also significant scattering by atmospheric aerosols over this spectral range. The solar angle (θ_o, ϕ_o) has a strong influence on T_d and E_s. These effects combine to provide a large amount of variability in the global spectral irradiance both in magnitude and spectral shape. For example, figure 1 plots three global irradiance spectra that were measured at the same location but at different times in Boulder, Colorado in the summer of 1997. The three spectra $L_1(\lambda), L_2(\lambda)$, and $L_3(\lambda)$ were measured on a sunny day, a partly cloudy day, and a humid cloudy day respectively. $L_2(\lambda)$ and $L_3(\lambda)$ have a lower magnitude due to the cloudy conditions and $L_3(\lambda)$ has the strongest water absorption feature due to high humidity. Figure 2 plots the three spectra from figure 1 after normalization to unit length and demonstrates the differences in spectral shape among the spectra.

For a matte surface the reflected radiance is the product of the surface reflectance and the global spectral irradiance

$$U(\lambda) = L(\lambda) R(\lambda) \quad (2)$$

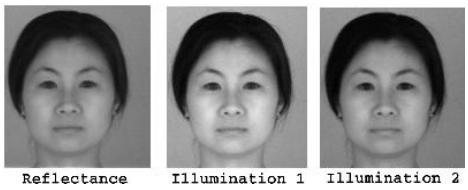

Figure 3. Pseudo-color face images under different near-infrared illumination conditions

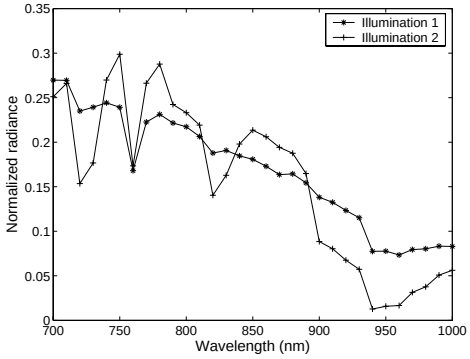

Figure 4. Normalized radiance spectra for forehead for illumination conditions shown in figure 3

where the global spectral irradiance $L(\lambda)$ will be referred to as an illumination function, $R(\lambda)$ is the intrinsic spectral reflectance of the surface material, and $U(\lambda)$ is the reflected radiance spectrum. Thus, the radiance $U(\lambda)$ varies as the illumination $L(\lambda)$ varies. For a calibrated hyperspectral camera the measured spectral radiance at a pixel will equal the reflected spectral radiance for the surface that images to that pixel. Figure 3 shows face images of a subject that were synthesized using a near-infrared spectral reflectance image and two different illumination functions $L_1(\lambda)$ and $L_2(\lambda)$ that were measured in Boulder in the summer of 1997. The color images were formed using red = 720nm, green = 750nm, and blue = 940nm. Figure 4 plots the reflected radiance spectra $U_1(\lambda)$ and $U_2(\lambda)$ that correspond to a small region on the forehead of the subject shown in figure 3. We see that the spectra are significantly different due to the illumination effects.

Suppose that $U_1(\lambda), U_2(\lambda), \ldots, U_M(\lambda)$ is a set of M radiance spectra for a certain material where the subscript denotes a particular set of environmental conditions. If the radiance spectra are sampled at W wavelengths, then each spectrum $U_i(\lambda)$ can be represented by the W-dimensional vector $\mathbf{U}_i = (U_i(\lambda_1), U_i(\lambda_2), \ldots, U_i(\lambda_W))^T$. Various researchers have used low-dimensional subspaces to model the spectral variation of outdoor illumination.[16, 17] Similarly we can approximate each $\mathbf{U}_i$ using

$$\mathbf{U}_i \approx \sum_{j=1}^{N} \sigma_{ij} \mathbf{r}_j \tag{3}$$

where the W-dimensional vectors $\mathbf{r}_j$ define a fixed N-dimensional basis for the M radiance vectors and the constants σ_{ij} are weighting coefficients.

The accuracy of the approximation in (3) is given by the squared error

$$E_i = \left\| \mathbf{U}_i - \sum_{j=1}^{N} \sigma_{ij} \mathbf{r}_j \right\|^2 \tag{4}$$

The total squared error over a set $\mathbf{U}_1, \mathbf{U}_2, \ldots, \mathbf{U}_M$ of radiance vectors for a given set of basis vectors is

$$E_T = \sum_{i=1}^{M} E_i \tag{5}$$

The singular value decomposition (SVD)[18] can be used to generate a set of orthonormal basis vectors $\mathbf{r}_1, \mathbf{r}_2, \ldots, \mathbf{r}_N$ from $\mathbf{U}_1, \mathbf{U}_2, \ldots, \mathbf{U}_M$ that minimize E_T for any N. For the SVD basis, the coefficients that minimize E_i for each U_i are given by $\sigma_{ij} = \mathbf{U}_i \cdot \mathbf{r}_j$.

Figure 5. One reflectance image and seven radiance images with different expressions and face orientations for one subject

3. HYPERSPECTRAL DATA ACQUISITION

3.1. Indoor Data Collection

We used a hyperspectral imaging system from Opto-Knowledge Systems, Inc. (OKSI) that uses a liquid crystal tunable filter[19] from Cambridge Research Instruments (CRI) and a scientific grade CCD camera for data collection. The images were acquired with 31 bands sampled every 10nm over the near-infrared (700nm-1000nm) with 468×494 pixel spatial resolution. Two standard spectralon reflectance panels with constant 99% and 2% reflectance can be used to transform the raw images from the camera into spectral reflectance images for analysis.[15]

We collected hyperspectral face images of 200 subjects indoors under controlled diffuse illumination. The first image in figure 5 is a single band of a spectral reflectance image of one subject. We represent each face image for recognition experiments using spectral reflectance vectors that are extracted from small facial regions. The squares that are overlayed on the images in figure 5 indicate the facial regions that are considered for each subject. Up to five facial regions corresponding to the forehead, left cheek, right cheek, hair, and lips are used for each subject depending on the visibility of the regions. The spectral reflectance vector $\mathbf{R}_t = (R_t(\lambda_1), R_t(\lambda_2), \ldots, R_t(\lambda_W))^T$ is estimated for each facial region by averaging over the pixels in the squares shown in figure 5 where t is one of the tissue types: f(forehead), lc(left cheek), rc(right cheek), h(hair), or l(lip).

3.2. Outdoor Data Collection

The calibration of hyperspectral cameras to measure spectral radiance[20] enables sensor measurements to be predicted using physical models. A FieldSpec Handheld spectroradiometer from Analytical Spectral Devices, Inc. (ASD) was used to calibrate the hyperspectral camera in this work to measure spectral radiance at every pixel in the image. The spectroradiometer is calibrated, NIST traceable, to measure radiance over the visible and near-infrared spectral range of 325-1075 nm with a 1.6 nm sampling interval. The FieldSpec Handheld spectroradiometer has a fixed 25° field of view. The hyperspectral imaging system produces the measurement

$$I(x, y, \lambda_k) = S(x, y, \lambda_k)U(x, y, \lambda_k) + O(x, y, \lambda_k) \tag{6}$$

at spatial coordinate (x, y) and wavelength λ_k where $U(x, y, \lambda_k)$ is the incoming radiance for pixel (x, y), $S(x, y, \lambda_k)$ is the system response, and $O(x, y, \lambda_k)$ is an offset that includes dark current and stray light. The goal of spectral radiance calibration is to transform the raw measurement $I(x, y, \lambda_k)$ to spectral radiance $U(x, y, \lambda_k)$. For images of white and black spectralon panels, we have

$$I_W(x, y, \lambda_k) = S(x, y, \lambda_k)U_W(\lambda_k) + O(x, y, \lambda_k) \tag{7}$$

$$I_B(x, y, \lambda_k) = S(x, y, \lambda_k)U_B(\lambda_k) + O(x, y, \lambda_k) \tag{8}$$

where $U_W(\lambda_k)$ and $U_B(\lambda_k)$ are the reflected radiance spectra for the white and black spectralon panels respectively. For a given illumination configuration we can make accurate measurements for $U_W(\lambda_k)$ and $U_B(\lambda_k)$ using the FieldSpec Handheld spectroradiometer. As shown in figure 6, the spectroradiometer was pointed at the center of the target when measuring radiance. It was positioned one foot away from the target to avoid shadows and to ensure that the spectralon panel fills the field of view of the spectroradiometer. For both the white and black spectralon panels, we measured the radiance five times over a short time interval. The measured radiance spectra were averaged to obtain $U_W(\lambda_k)$ and $U_B(\lambda_k)$.

Figure 6. Radiance measurement using ASD FieldSpec Handheld spectroradiometer

Figure 7. Outdoor images taken at different times and different locations

We averaged 10 hyperspectral images of the white and black spectralon panels to obtain estimates of $I_W(x, y, \lambda_k)$ and $I_B(x, y, \lambda_k)$. These estimates are used together with (6) - (8) to get

$$U(x, y, \lambda_k) = \frac{(I(x, y, \lambda_k) - I_B(x, y, \lambda_k))U_W(\lambda_k)}{I_W(x, y, \lambda_k) - I_B(x, y, \lambda_k)} + \frac{(I_W(x, y, \lambda_k) - I(x, y, \lambda_k))U_B(\lambda_k)}{I_W(x, y, \lambda_k) - I_B(x, y, \lambda_k)} \tag{9}$$

Thus, we can obtain spectral radiance $U(x, y, \lambda_k)$ at each pixel in an image. We performed this calibration step at the beginning of each imaging session.

We collected outdoor hyperspectral images of ten subjects over a one month period. The images were taken in five different sessions with various natural illumination conditions. Figure 5 shows a single band of an indoor reflectance image and seven outdoor radiance images for one subject. For the outdoor radiance images, two front-view images were taken with neutral expression (fog and foa). Another front-view image (fob) was taken with a different expression. Four other images were taken with face orientations of -90°, -45°, 45°, and 90°, which are referred to as for2, for1, fol1, and fol2 respectively. Figure 7 shows a single band of four images of one subject taken during four different imaging sessions. The four images were acquired at different imaging locations and under different illumination conditions. For each imaging session, the images were acquired in sets of seven images per subject as illustrated by the seven radiance images shown in figure 5.

4. SPECTRAL METRIC FOR FACE RECOGNITION

Given a reflectance vector $\mathbf{R}_t(i)$ for tissue type t of subject i and a set of M illumination spectra, we can generate a set of N orthonormal basis vectors $\mathbf{b}_{t1}(i), \mathbf{b}_{t2}(i), \ldots, \mathbf{b}_{tN}(i)$ that represent the space of reflected radiance vectors for this subject and tissue type for any N using the method described in section 2. Since there is often specular reflection from human faces under outdoor illumination, we add an additional vector $\overline{\mathbf{L}}$ to the N-dimensional linear subspace for each subject i for each tissue type. $\overline{\mathbf{L}}$ is the average vector of the illumination vector set $\mathbf{L}_1, \mathbf{L}_2, \ldots, \mathbf{L}_M$. Thus, for the purpose of modeling specular reflection we are approximating the illumination spectrum by the average over the illumination vector set and using the constraint that the specular reflectance for skin is nearly constant spectrally over the wavelength range that we are considering. After orthogonalization, we get a $(N+1)$-dimensional linear subspace $\mathbf{b}_{t1}(i), \mathbf{b}_{t2}(i), \ldots, \mathbf{b}_{tN}(i), \mathbf{b}_{tN+1}(i)$ where $\mathbf{b}_{tN+1}(i)$ is the normalized difference vector between $\overline{\mathbf{L}}$ and its projection onto the N-dimensional linear subspace.

Given an image of subject j that is acquired under unknown illumination denote the normalized reflected radiance for tissue type t by the column vector $\overline{\mathbf{U}}_t(j)$. We can approximate the vector $\overline{\mathbf{U}}_t(j)$ using the $(N+1)$-dimensional linear subspace for tissue type t for subject i as

$$\overline{\mathbf{U}}_t(j) \approx \sum_{n=1}^{N+1} (\overline{\mathbf{U}}_t(j) \cdot \mathbf{b}_{tn}(i))\mathbf{b}_{tn}(i) = \widehat{\mathbf{U}}_t(i, j) \tag{10}$$

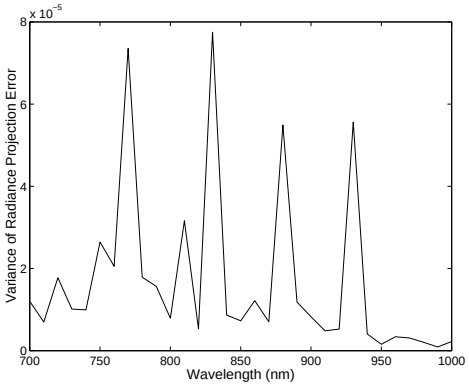

Figure 8. Variance of forehead radiance projection error as a function of wavelength

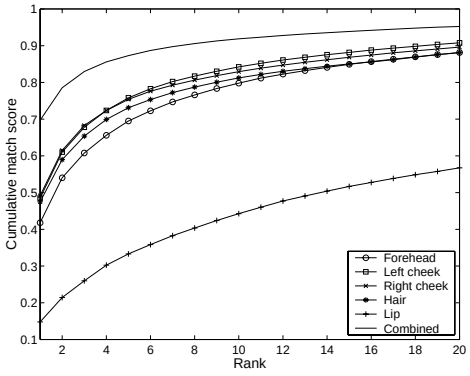

Figure 9. Identification performance of front view probes using simulated data

where $\widehat{\mathbf{U}}_t(i,j)$ is the projection of $\overline{\mathbf{U}}_t(j)$ onto the subspace for subject i. The distance from $\overline{\mathbf{U}}_t(j)$ to the model for subject i for tissue type t is defined by the square of the Mahalanobis distance[21]

$$D_t(i,j) = \left(\overline{\mathbf{U}}_t(j) - \widehat{\mathbf{U}}_t(i,j)\right)^T \Sigma_t^{-1} \left(\overline{\mathbf{U}}_t(j) - \widehat{\mathbf{U}}_t(i,j)\right) \tag{11}$$

where Σ_t is the covariance matrix for the distribution of the error between the reflected radiance vector $\overline{\mathbf{U}}_t(i)$ for a subject i and $\widehat{\mathbf{U}}_t(i,i)$. The distance in (11) can be generalized to consider all visible tissue types. We define the distance between a spectral radiance image of subject j and the model for subject i by

$$D(i,j) = \omega_f D_f(i,j) + \omega_{lc} D_{lc}(i,j) + \omega_{rc} D_{rc}(i,j) + \omega_h D_h(i,j) + \omega_l D_l(i,j) \tag{12}$$

where ω_t is 1 if tissue type t is visible in the image of subject j and 0 otherwise.

For our experiments, the covariance matrix Σ_t is estimated using the database of radiance face images. For every radiance image of subject i we compute the error vector $\overline{\mathbf{U}}_t(i) - \widehat{\mathbf{U}}_t(i,i)$. These error vectors are used to estimate the covariance matrix $\Sigma_t(i)$. For efficiency we only consider the diagonal elements of $\Sigma_t(i)$ and set the off-diagonal elements to zero. The matrix Σ_t that is used in (11) is obtained by averaging the diagonal matrices $\Sigma_t(i)$ over all subjects i. Figure 8 plots the diagonal elements of Σ_t as a function of wavelength for the forehead tissue type. The Σ_t matrix was estimated using 63 radiance images of 10 subjects. As seen in figure 8, the variance has larger values at specific bands such as 760 nm and 930 nm. This is due primarily to variability in the atmospheric absorption of oxygen and water vapor at these bands. The diagonal elements of Σ_t for other tissue types have a similar appearance.

5. RECOGNITION EXPERIMENTS

5.1. Simulated Images

The recognition experiments consider a database of 200 subjects. For each subject, the indoor gallery image fg was used to obtain the reflectance spectra for all five tissue types. We used a database[22] of 7258 outdoor illumination spectra to synthesize reflected radiance spectra for each tissue type for each subject. For each of the 200 subjects, a low dimensional linear subspace for the radiance spectra for each tissue type was generated to model variability due to illumination. A subspace dimensionality of four for all tissue types for all subjects provided the best recognition performance and was used for the experiments. These subspaces are the only information that is used to represent the 200 subjects in the gallery.

The face recognition experiments were first conducted using simulated radiance images. A total of 1200 near-infrared spectral reflectance images were used that consider six images of each of the 200 subjects. The six

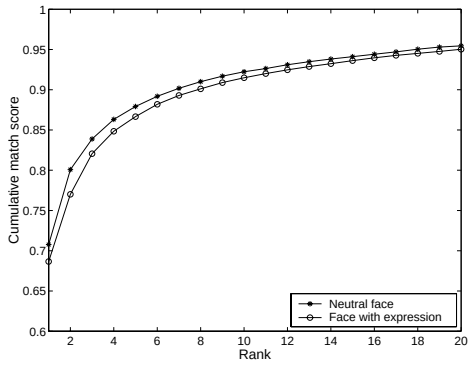

Figure 10. Performance comparison of probes with and without facial expression using simulated data

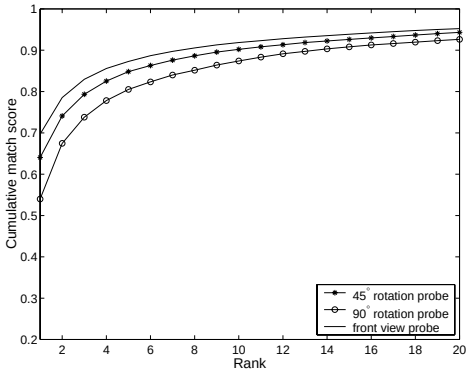

Figure 11. Identification performance of rotated face images using simulated data

images correspond to two frontal images (neutral expression and non-neutral expression) that are distinct from fg and four images that were acquired using the different face orientations shown in figure 5. For each of the 1200 reflectance images we synthesized 100 radiance images by multiplying each reflectance image by 100 randomly selected illumination spectra from the illumination database. Each radiance image j was compared with each of the 200 subjects i in the gallery using the distance $D(i,j)$ of (12). The radiance image was declared by the system to be an image of the gallery subject i for which $D(i,j)$ is the smallest. We present the experimental results using cumulative match scores.[6] Each experiment considers a gallery of known subjects and a set of probe images of unknown subjects. The cumulative match score at rank r for an experiment is the fraction of probe images for which the correct match in the gallery is one of the top r matches that the system finds in the gallery for the probe image.

The first experiment uses the synthesized frontal probes foa and fob to examine the accuracy of hyperspectral face recognition over variation in illumination. This experiment considers using the distance of (11) for each tissue type individually as well as the distance of (12) that uses all five tissue types. Figure 9 plots the cumulative match score functions that are obtained when using $D_t(i,j)$ for each tissue type individually and $D(i,j)$ for the combination of all tissue types. We see that the cheeks and forehead are the most useful of the individual tissue types while the lip is the least useful. The recognition rate is significantly improved when all tissue types are utilized with about 70% of the probes correctly recognized as the best match and more than 91% correctly identified in the top 10 matches. A total of 40000 probes were used in this experiment.

The two curves in figure 10 compare the recognition performance for foa and fob probes when all tissue types are considered. The foa probe images have the same neutral facial expression as the gallery images which were used to generate the linear radiance subspaces. The fob probes have different expressions which are usually smiles. We see that there is little degradation in performance due to change of expression.

Figure 11 examines recognition performance when variation in both illumination and face orientation are present. A recent study has shown that when using geometric features for recognition there is performance degradation when head pose variation and illumination variation are combined.[12] In figure 11 we see that for probes that are rotated 45° to the left or right from the frontal gallery image, more than 64% of the probes are correctly recognized as the best match and about 90% have the correct match ranked in the top 10. For the difficult case of probes rotated 90° about 54% and 87% of the probes have the correct match ranked as the top 1 and in the top 10 respectively. These results are promising for face recognition under unknown outdoor illumination and with varying face orientation. The distance function defined in terms of all visible tissue types was used to generate the results in figure 11. For each of the three curves in figure 11, a total of 40000 probes were used for the experiment.

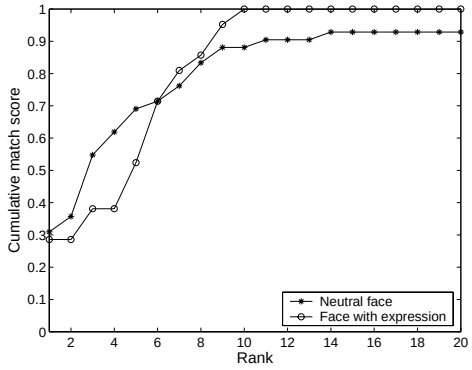

Figure 12. Performance comparison of probes with and without facial expression using real data

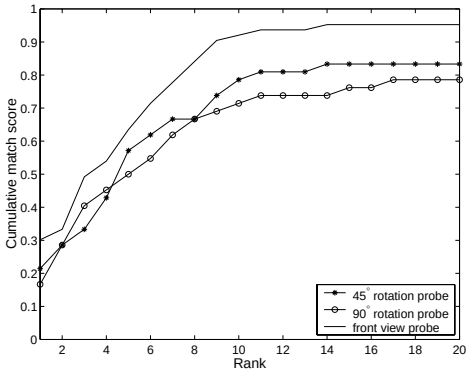

Figure 13. Identification performance of rotated face images using real data

5.2. Real Outdoor Images

Among the 200 subjects, 10 subjects were imaged outdoors under unknown natural illumination. There were five outdoor imaging sessions over a one month period at different locations and under different conditions. Each subject was imaged in one to four imaging sessions. Figure 7 shows a single band of the image of one subject from four different imaging sessions. At each imaging session, three front view images and four rotated face images of each subject were acquired as shown in figure 5. The seven images of one subject is called an outdoor image set. A total of 21 outdoor image sets were collected. The images were calibrated to spectral radiance using the procedure described in section 3.3.2. The 200 gallery subjects used in this outdoor study are the same as in the simulated data experiments except for two subjects. These two were newly recruited for the outdoor study. Two randomly selected subjects from the original gallery set were replaced by these two new subjects.

Face recognition experiments similar to those described in section 5.5.1 were conducted for the real outdoor images. The frontal probes fog, foa and fob were used to examine the performance of the algorithm in the presense of variable expressions and the results are presented in figure 12. These results consider the utilization of all tissue types. The fog and foa images have the same neutral facial expression as the gallery images fg. The fob images typically have smiling expressions. For both cases, about 30% of the probes are correctly recognized at rank 1 and over 80% are recognized correctly at rank 10. This experiment considers 42 probes with neutral expression and 21 probes with non-neutral expression.

Figure 13 examines the extent of performance degradation when introducing variations in both illumination and face orientation. In figure 13 we see that for probes that are rotated 45°, more than 79% of the probes have the correct match ranked within the top 10. For the more difficult case of 90° rotated faces, about 71% of the probes have the correct match ranked in the top 10. This experiment considers 42 probes with 45° face rotation and 42 probes with 90° face rotation. There is degradation compared to the simulated data, especially for the recognition rate of the best match. However these results are promising for face recognition under unknown outdoor illumination and with various face orientations.

6. CONCLUSION

We have tested the utilization of hyperspectral imaging for face recognition with changes in head pose and facial expression when the illumination is unknown. The experiments considered a database of near-infrared (0.7μm-1.0μm) hyperspectral images for 200 subjects. A set of 7258 global spectral irradiance functions was used to synthesize reflected radiance images of each subject. A low-dimensional linear model for each tissue type for each subject was used to model illumination variation in radiance images. We conducted recognition experiments using simulated radiance images as well as real radiance images taken outdoors. We collected reflected spectral radiance images for 10 of the 200 subjects. The radiance images were taken on different days over a one month period under unknown outdoor illumination. Hyperspectral radiance images with different facial expressions

and face rotations were recognized by projecting the reflected radiance spectra of different tissue types onto linear subspace representations for the 200 subjects. There is some degradation of recognition performance from simulated data to real data for each experiment. This is possibly caused by irregular shadows on the face under natural illumination and by instrument calibration issues. Nevertheless, for both datasets, the algorithm provides accurate recognition performance for front view probes with or without facial expression changes. The recognition rate for probes rotated up to 90° is also promising even though the probes were imaged on different days and under unknown outdoor illumination.

Acknowledgment

This work has been supported by the DARPA Human Identification at a Distance Program through AFOSR Grant F49620-01-1-0058. This work has also been supported by the Laser Microbeam and Medical Program (LAMMP) and NIH Grant RR01192. The indoor data was acquired at the Beckman Laser Institute on the UC Irvine campus. The authors would like to thank J. Stuart Nelson and Montana Compton for their valuable assistance in the process of IRB approval application and human subjects recruitment.

REFERENCES

1. K. Etemad and R. Chellappa, "Discriminant Analysis for recognition of human face images," J. Opt. Soc. Am. A **14**, 1,724–1,733 (1997).
2. B. Moghaddam and A. Pentland, "Probabalistic Visual Recognition for Object Recognition," IEEE Trans. Pattern Anal. Machine Intell. **19**, 696–710 (1997).
3. D. Swets and J. Weng, "Using Discriminant eigenfeatures for image retrieval," IEEE Trans. Pattern Anal. Machine Intell. **18**, 831–836 (1996).
4. J. Wilder, "Face recognition using transform coding of grayscale projection and the neural tree network," in *Artifical neural networks with applications in speech and vision*, R. Mammone, ed. (Chapman Hall, 1994), pp. 520–536.
5. L. Wiskott, J.-M. Fellous, N. Kruger, and C. von der Malsburg, "Face recognition by elastic bunch graph matching," IEEE Trans. Pattern Anal. Machine Intell. **19**, 775–779 (1997).
6. P. Phillips, H. Moon, A. Rizvi, and P. Rauss, "The FERET evaluation methodology for face-recognition algorithms," IEEE Trans. Pattern Anal. Machine Intell. **22**, 1090–1104 (2000).
7. P. Phillips, P. Grother, R. Micheals, D. Blackburn, E. Tabassi, and M. Bone, "Face Recognition Vendor Test 2002: Overview and Summary," Tech. rep., Defense Advanced Research Projects Agency (2003).
8. Y. Adini, Y. Moses, and S. Ullman, "Face recognition: the problem of compensating for changes in illumination direction," IEEE Trans. Pattern Anal. Machine Intell. **19**, 721–732 (1997).
9. A. Georghiades, P. Belhumeur, and D. Kriegman, "From few to many: illumination cone models for face recognition under variable lighting and pose," IEEE Trans. Pattern Anal. Machine Intell. **23**, 643–660 (2001).
10. R. Ishiyama and S. Sakamoto, "Geodesic illumination basis: compensating for illumination variations in any pose for face recognition," in *Proc. Int. Conf. on Patt. Recog.* pp. 297–301 (2002).
11. D. Socolinsky and A. Selinger, "A comparative analysis of face recognition performance with visible and thermal infrared imagery," in *Proc. Int. Conf. on Patt. Recog.* (2002).
12. R. Gross, J. Shi, and J. Cohn, "Quo vadis face recognition?" Tech. Rep. CMU-RI-TR-01-17, Robotics Institute, Carnegie-Mellon University (2001).
13. G. Healey and D. Slater, "Models and Methods for Automated Material Identification in Hyperspectral Imagery Acquired under Unknown Illumination and Atmospheric Conditions," IEEE Trans. Geosci. Remote Sensing **37**, 2706–2717 (1999).
14. "Machine vision sees the food contaminants we can't see," Agricultural Research **50**, 4–8 (2002).
15. Z. Pan, G. Healey, M. Prasad, and B. Tromberg, "Face recognition in hyperspectral images," IEEE Trans. Pattern Anal. Machine Intell. **25**, 1552–1560 (2003).
16. D. Judd, D. MacAdam, and G. Wyszecki, "Spectral distribution of typical daylight as a function of correlated color temperature," J. Opt. Soc. Am. **54**, 1031–1040 (1964).

17. D. Slater and G. Healey, "Analyzing the Spectral Dimensionality of Outdoor Visible and Near-infrared Illumination Functions," J. Opt. Soc. Am. **15**, 2913–2920 (1998).
18. G. Golub and C. van Loan, *Matrix Computations* (Johns Hopkins University Press, Baltimore, MD, 1983).
19. N. Gat, "Imaging Spectroscopy using tunable filters: a review," in *SPIE Proceedings 4056, Wavelet Applications VII*, H. H. Szu, M. Vetterli, W. J. Campbell, and J. R. Buss, eds., pp. 50–64 (2000).
20. T. Chrien, R. Green, and M. Eastwood, "Accuracy of the spectral and radiometric laboratory calibration of the Airborne Visible/Infrared Imaging Spectrometer (AVIRIS)," in *SPIE Proceedings 1298, Imaging Spectrometry of the Terrestrial Environment*, C. Banninger, ed., pp. 37–49 (1990).
21. R. Duda, P. Hart, and D. Stork, *Pattern Classification* (Wiley-Interscience, New York, 2001), 2nd edition.
22. Z. Pan, G. Healey, and D. Slater, "Global spectral irradiance variability and material discrimination at Boulder, Colorado," J. Opt. Soc. Am. A **23**, 513–521 (2003).